Chinese Chemical Letters 33 (2022) 1407–1411

Contents lists available at ScienceDirect

Chinese Chemical Letters

journal homepage: www.elsevier.com/locate/cclet

"Series and parallel" design of ether linkage and imidazolium cation synergistically regulated four-armed polymerized ionic liquid for all-solid-state polymer electrolyte

Zehui Xie[a], Yang Zhou[a,b], Canhui Ling[a], Xinlin Zhu[a], Zhao Fang[a], Xiaolong Fu[c], Wuwei Yan[d], Yong Yang[a,*]

[a] Key Laboratory of Soft Chemistry and Functional Materials, Ministry of Education, School of Chemistry and Chemical Engineering, Nanjing University of Science and Technology, Nanjing 210094, China
[b] The Green Aerotechnics Research Institute of Chongqing Jiaotong University, Chongqing 401120, China
[c] Xi'an Modern Chemistry Research Institute, Xi'an 710065, China
[d] Shenzhen BTR Nanotechnology Company, Ltd., Shenzhen 518106, China

ARTICLE INFO

Article history:
Received 8 June 2021
Revised 10 July 2021
Accepted 7 August 2021
Available online 12 August 2021

Keywords:
Series and parallel
Polymer electrolyte
All-solid-state
Lithium metal battery
Four-armed

ABSTRACT

Developing all-solid-state polymer electrolytes (SPEs) with high electrochemical performances and stability is of great importance for exploiting of high energy density and safe batteries. Herein, ether linkage and imidazolium ionic liquid (ILs) are incorporated into the multi-armed polymer backbone though the series and parallel way. The parallel polymeric ionic liquid (P-P (PEGMA-IM)) maximizes the synergistic effect of ILs and ether linkage, which endowed the material with low crystallinity and high flame retardancy. The P-P (PEGMA-IM) based P-SPE presents a high ionic conductivity of 0.489 mS/cm at 60 °C, an excellent lithium-ion transference number of 0.46 and a wide electrochemical window of 4.87 V. The assembled lithium metal battery using P-SPE can deliver a capacity of 151 mAh/g at 0.2 C, and the capacity retention ratio reaches 82% with a columbic efficiency beyond 99%. The overpotential of P-SPE based symmetric battery is 0.08 V, and there is no apparent magnifying even after 130 h cycling. This new design provides a new avenue for exploitation of advanced SPEs for the next-generation batteries.

Traditional lithium-ion batteries (LIBs) present several drawbacks, such as safety issues, unsatisfied energy density, weak flexibility, though they have been widely used and respected as the first choice for energy storage device nowadays [1–3]. In particular, the generally used organic liquid electrolyte significantly hinders the practical applications of some high capacity electrodes. The problems of leakage, environmental pollution, combustion and explosion also require to be overcome [4–7].

As a promising tactic to deal with the above-mentioned conundrums, solid-state polymer electrolytes (SPEs) have aroused great research enthusiasm owing to their flexibility and facile tailored feature [8–11]. Since the discovery of ion conductivity in polyethylene oxide (PEO), it has been comprehensively studied owing to the fundamental role of ether linkage $(\text{-CH}_2\text{-CH}_2\text{-O-})_n$ in the backbone [12]. The oxygen (O) atom in this unit presents a high donor number for Li^+, which provides the driving force for ion transport. In addition, the high dielectric constant ($\varepsilon \approx 5$) of ether linkage facilitates the ion-pair dissociation in the Li salts, promoting the solvation of Li^+ [13–15]. Nonetheless, the major challenge is that Li-ion migration is commonly restricted by the crystalline region in PEO, and the resulted low ionic conductivity ($\sim 10^{-7}$ S/cm at room temperature) fails to suffice practical application [16–19]. The flammability and low critical current density of PEO and most other SPEs also notoriously hinder their applications [20–23]. To date, numerous efforts have been made to enhance the ionic conductivity of PEO-based SPEs in order to utilize the advantages of the ether linkage. Various inorganics (Al_2O_3, TiO_2, $Li_7La_3Zr_2O_{12}$, *etc.*) [24–26] and organics (PU, PPO, PVP, *etc.*) [4,27,28] have been added into PEO matrix, and the crystallinity of PEO is effectively decreased. However, there is only weak interactions between these fillers and PEO by the physical blending. The superiorities of the ether linkage cannot be fully presented.

Incorporation of the ether linkage into the advanced functional polymers *via* chemical bonding can combine the merits of the respective constituents and maximize the synergy effects of the different units [15,29,30]. In this context, PEO derived block copolymers, grafted polymers and crosslinking networks were prepared

* Corresponding author.
E-mail address: yychem@njust.edu.cn (Y. Yang).

https://doi.org/10.1016/j.cclet.2021.08.031
1001-8417/

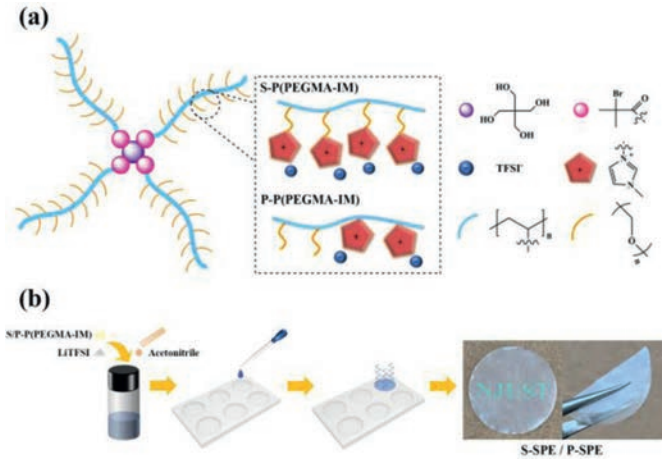

Fig. 1. (a) Illustration of the structural difference between series and parallel polymers. (b) Figmatic illustration of the fabrication of SPEs.

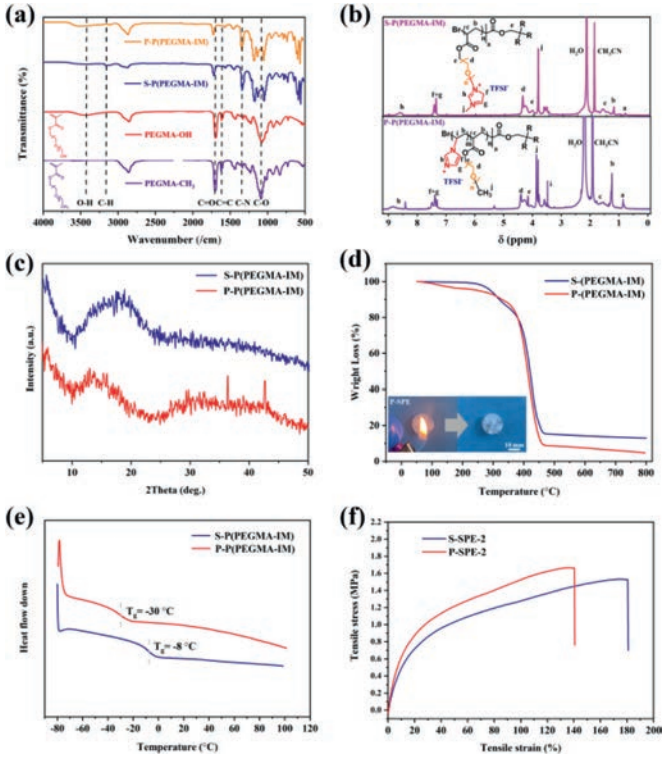

Fig. 2. (a) FTIR, (b) ^{1}H NMR, (c) XRD, (d) TGA (Inset is the P-SPE exposed to a flame), (e) DSC and (f) stress-strain tests of the series and parallel samples.

and investigated as SPEs. Among them, the multi-armed structure can suppress the crystallization of polymer chains easily, leading to increase of the amorphous regions and the improved ionic conductivity. Our group has prepared four-armed tetraalkylammonium and imidazolium based polymeric ionic liquid (PILs) as the solid-state electrolyte, the electrochemical and battery performances are all improved by virtue of the special macromolecular structure and the merits of PILs (high conductivity, nonflammable, thermal stability, *etc.*) [31]. However, to the best of our knowledge, there is rare example on the combination of PILs with ether linkage. Since the introduction of ether groups can result in the change of intra- and intermolecular interactions of a system [32], the combination mode of ether linkage with PILs should be tuned for optimized electrochemical performance.

Herein, we firstly incorporate ether linkage from poly(ethylene glycol) monomethacrylate-OH (PEGMA-OH) and poly(ethylene glycol) monomethacrylate-CH_3 (PEGMA-CH_3) into the multi-armed imidazolium-based PILs. In the S-P(PEGMA-IM) with series structure, imidazolium cation is hanged on the ether linkage. In comparison, when the two functional units are distributed separately on different branches, the parallel structure (P-P(PEGMA-IM)) is defined. For the electrochemical measurements, P-P(PEGMA-IM) derived SPE shows the higher ion conductivity, Li^+ transference number and stability than that of the S-P(PEGMA-IM). After assembling Li metal batteries, the P-P(PEGMA-IM)-based LMBs present higher specific capacity, better cycling stability, and superior rate performance. These improvements and the corresponding mechanism attributable to the parallel structure are investigated in detail.

The four-armed polymers based on PEGMA-OH and PEGMA-CH_3 were synthesized *via* the atom transfer radical polymerization (ATRP) with the as-prepared initiator. Accordingly, S-P(PEGMA-IM) was obtained from bromination, imidazolium grafting and ion exchange for PPEGMA-OH. P-P(PEGMA-IM) was developed by subsequent ATRP of vinyl imidazole, bromination and ion exchange on PPEGMA-CH_3. The detailed procedure is shown in Text S2 and Fig. S1 (Supporting information). The structural disparity between S-P (PEGMA-IM) and P-P (PEGMA-IM) can be well defined in Fig. 1a. The fabrication of SPEs based on series and parallel polymers is illustrated in Fig. 1b *via* a solvent casting technique, and the translucent and flexible membranes can be obtained ultimately.

To verify the structure of S-P(PEGMA-IM) and P-P (PEGMA-IM), FTIR and ^{1}H NMR tests are conducted and displayed in Figs. 2a and b. The peaks at 1640 cm^{-1} can be assigned to the stretching vibration of C=C in the PEGMA-based monomers. In contrast, the peaks vanish from the spectra of polymers, suggesting the thorough polymerization. The broad absorption around 3250-3600 cm^{-1} demonstrates the existence of -OH in PEGMA-OH, where as it cannot be found in S-P(PEGMA-IM). The presence of a peak at 1350 cm^{-1} is originated from the C-N, which declares the successful integration of imidazolium. Additionally, the characteristic peaks at 1740 cm^{-1} are attributed to C=O, while the absorption at 3140 cm^{-1} and 2950 cm^{-1} can be, respectively designated to the unsaturated and saturated stretching vibration of C-H. Moreover, the successful introduction of $TFSI^-$ is validated by the peaks at 1130, 1050, 740 and 567 cm^{-1}, which agrees well with previously reports [33,34]. In the ^{1}H NMR, peaks at 1.4 ppm and 1.8 ppm further verify the polymerization of C=C bond, whose characteristic signal commonly appears at lower field. Imidazolium's proton signals present at 7.4 and 8.7 ppm. Meanwhile, the peaks at 4.4 ppm, 4.2 ppm and 3.8 ppm are corresponding to -O-CH_3, -N-CH_2- and N-CH_3, respectively. In particular, the two samples can be distinguished by the peaks around 0.9 ppm, where P-P(PEGMA-IM) manifests strong signal due to the additional -CH_3 linked to the ether chain. The molecular weight of S-P(PEGMA-IM) and P-P(PEGMA-IM) can also be calculated to be 75,000 and 61,000 based on the integral areas in ^{1}H NMR as shown in Fig. S2 (Supporting information).

The crystallinity of series and parallel PILs were studied *via* XRD. As shown in Fig. 2c, the two samples display analogical diffraction patterns, where a diffusion peak at $2\theta = 21°$ and a wide diffraction within the range of $2\theta = 30°–41°$ can be observed. What is noticeable is that contrasted with S-P(PEGMA-IM), P-P(PEGMA-IM) exhibits weaker diffraction intensity, indicating a decreased crystallinity in the parallel configuration which is conducive to the transportation of Li^+.

TGA was adopted to clarify the thermostability of the two PILs. As it can be seen in Fig. 2d, the trivial weight loss below 200 °C is owing to the moisture. Apparently, the two samples exhibit similar profiles and a thermo stability up to 260 °C, which mainly stems

from the virtually identical four-arm configuration and chemical composition. From the inset, it is well observed that P-SPE is flame retardant and can mitigate the safety hazard against flaming. Glass transition temperature (T_g) is a critical property that intimately related to the crystallinity of polymer, further manipulating the Li^+ migration. DSC characterizations were thus conducted to probe into the phase evolution and T_g of the PILs, and the corresponding profiles are revealed in Fig. 2e. There is apparently no melting peaks below 100 °C in both PILs, suggesting the as-prepared polymer are amorphous, which coordinates with the result of XRD. In addition, T_g of the PILs can be indicated by the descending point of the curve, where P-P(PEGMA-IM) exhibits a T_g of -30 °C, lower than that of S-P(PEGMA-IM). This may be ascribed to the imidazolium branched onto the polymer backbone, which prohibits the close-packing of ether linkage in PEGMA.

Mechanical strength is a fundamental feature for SPEs, which can be efficacious in suppressing dendrite growth. Stress-strain tests were accordingly carried out (Fig. 2f). S-SPE exhibits a fracture stress of 1.52 MPa when applied to the maximum strain of 180.6%. Contrastively, an enhanced fracture stress of 1.66 MPa at the maximum strain of 140.7% is rendered by P-SPE. This indicates that P-SPE is more durable against the dendrites growth. The block polymerization of PEGMA-CH_3 and imidazolium resulted in the close interaction between them, interrupting the crystallinity of ether linkage. Moreover, the increased intermolecular interactions and physical cross-links can be endowed. This strengthens the fracture stress for P-SPE. Despite that, the elongation degree is undermined compared with S-SPE, because the slip between polymer segments becomes difficult. The moderate mechanical strength ($\sim 10^6$ Pa) of both SPEs is tough enough to suppress dendrite growth when utilized in lithium metal battery according to the previous literature [35].

Electrochemical impedance spectroscopy (EIS) was conducted in order to make a thorough inquiry into the impact of temperature and content of lithium salt on the ionic conductivity of SPEs. The temperature dependence of the ionic conductivities of both SPEs with incremental lithium salt loading was depicted in Fig. 3a and Fig. S3 (Supporting information). As can be noted, the maximum ionic conductivity is reached with 20 wt% LiTFSI for both S-SPE and P-SPE. The ionic conductivity ceases to increase as LiTFSI is further added, the culprit of which may be the effect of charge accumulation brought by the excessive amount of lithium salts [36]. Regarding the temperature, a quantitative relationship can be concretized by Vogele Tammane Fulcher (VTF) equation (Eq. S2 in Supporting information). According to Eq. S2, the activation energy (E_a) of each SPE can be calculated (Table S1 in Supporting information). The ionic conductivity has a notably inverse relationship with E_a, which can also be extrapolated from the equation. At the optimal content of lithium salt, P-SPE exhibits an ionic conductivity of 7.91×10^{-5} S/cm at room temperature, three times of the series one. Additionally, an ameliorated ionic conductivity of 0.489 mS/cm can be monitored at 60 °C owing to the phase changing to a more amorphous state, which confers extra entropy and free volume for segment motion [12]. The relatively lower E_a (3.1~4.2 kJ/mol) for P-SPE also denotes a declined energy barrier for Li transportation. The mechanism of Li^+ transport in the two topologies is demonstrated in Fig. 3e. The enhanced ion conduction in P-SPE is majorly originated from the formation of a "green channel" based on the well-organized ether-linkage and imidazolium regions. As emphasized in the framed up region, the dissociated Li^+ can facilely enter in the low crystalline ether-linkage region for fast transfer without the hindrance of imidazolium groups. Regarding the series structure, the coordination between Li^+ and the ether linkage requires squeezing of Li^+ into the closely packed segments of PEGMA. The migration of Li^+ will be interrupted by the widely distributed imidazolium groups.

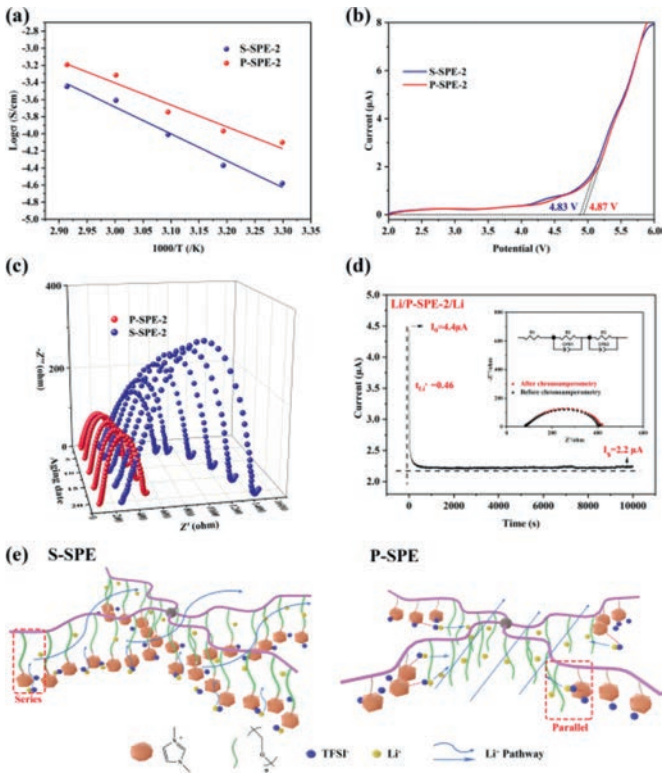

Fig. 3. (a) Ionic conductivity of S-SPE and P-SPE at different temperatures. (b) Electrochemical windows test of S-SPE and P-SPE at 60 °C. (c) Impedance profiles for Li/SPE/Li cells assembled by S-SPE and P-SPE over different aging period at 60 °C. (d) Chronoamperometry profile and AC impedance spectra (inset) before and after polarization for Li/SPE/Li cells with P-SPE at 60 °C. (e) The mechanism of Li^+ conduction in S-SPE and P-SPE.

Considering one of the major inadequacies of SPE is the weak chemical stability against high-energy-density cathodes, a wide electrochemical window is extraordinarily appreciated. In this case, the electrochemical stability of S-SPE and P-SPE was investigated *via* linear sweep voltammetry (LSV) at 60 °C, as is demonstrated in Fig. 3b. A tardy increment of the current density is observed when the voltage applied on the electrodes escalates, and the current intensity significantly increased as the voltage exceeded 4.5 V. After curve fitting, the oxidative degradation points of the two SPEs can be identified. The point starts at approximately 4.83 V for the S-SPE and 4.87 V for the P-SPE, suggesting the two SPEs are stable up to 4.8 V.

To further probe into the interfacial compatibility and stability between the Li metal and SPEs, Li/SPE/Li symmetric battery was assembled, which was subsequently examined to clarify the resistance transmission at different storage time. As displayed in Fig. 3c, the brief profile of the resistance curves are semicircles. According to the classic theory [37], bulk resistance (R_b) of the SPEs and the interfacial resistance (R_f) between the electrolyte and electrode are obtainable, corresponding to the initial and span values of the semicircles. The R_b of the S-SPE and P-SPE are 276 Ω and 85 Ω, respectively. Also, it is apparent that R_f of both electrolytes increase upon the aging process. This can be attributed to the infiltration of the electrolyte into the electrode as the prolonging of storage time, when a passivation layer is generated and the interfacial impedance then increases. It is worth noting that the R_f of S-SPE is evidently higher than that of P-SPE, and the R_f increment of S-SPE is also more obvious compared to P-SPE whose R_f remains quite stable with a sluggish increase from 317 Ω to 396 Ω during the 20-day's aging. This suggests the interfacial compatibility

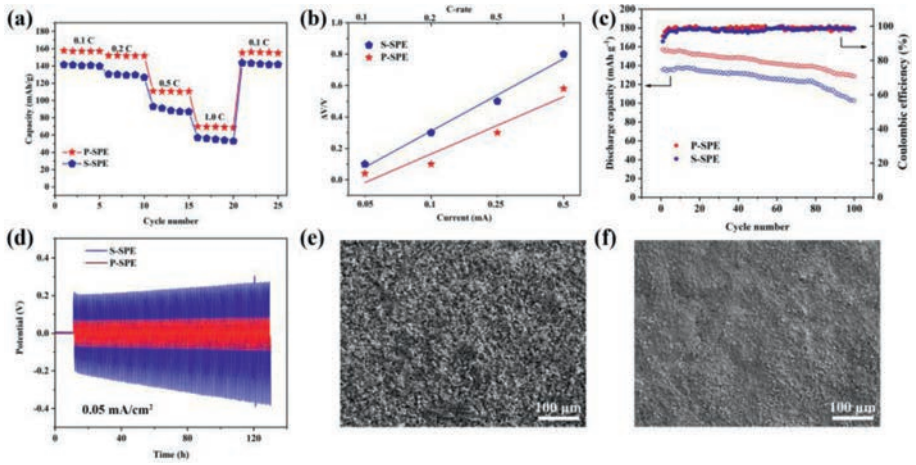

Fig. 4. Electrochemical performance of Li/$LiFePO_4$ batteries at 60 °C assembled with S-SPE and P-SPE: (a) rate performance, (b) voltage distance between the charge and discharge curves, (c) cycle stability at 0.2 C. (d) Polarization tests for symmetric Li/S-SPE/Li and Li/P-SPE/Li batteries. (e, f) SEM images of the surface of lithium electrode after polarization tests for S-SPE and P-SPE.

of P-SPE is more prominent than S-SPE when contacted with the electrode.

Moreover, the transference number of lithium ion (t_{Li^+}) was studied *via* chronoamperometry and electrochemical impedance spectroscopy (EIS) as described in the experimental section. The equivalent circuit is simulated accordingly. For Li/S-SPE/Li symmetric cell (Fig. S4 in Supporting information), the I_0 and I_s are measured to be 3.2 μA and 1.2 μA, and the R_0 and R_s are 600 Ω and 650 Ω, respectively. The t_{Li^+} can be calculated to be 0.41 based on Eq. S3 (Supporting information). Whereas the t_{Li^+} for the Li/P-SPE/Li cell (Fig. 3d) turns out to be 0.46. The high t_{Li^+} of the two SPEs is mainly attributable to the multi-armed topologies which significantly decreased the crystallinity of polymers compared with the linear counterpart. Additionally, the imidazolium cations have electrostatic interactions with $TFSI^-$ anions, partly prohibiting the motion of the anions and thus enhancing the t_{Li^+}. The parallel structure is more favorable for ion transference majorly owing to the synergistic effect of imidazolium groups and ether linkage.

$LiFePO_4$/Li batteries using lithium anode and $LiFePO_4$ as cathode was assembled to evaluate the overall performance of these two SPEs. Fig. 4a shows the rate performance of batteries using different SPEs. The discharge capacity of Li/P-SPE/$LiFePO_4$ can reach 157 mAh/g, 151 mAh/g, 110 mAh/g and 70 mAh/g at 0.1 C, 0.2 C, 0.5 C and 1 C, respectively. While Li/S-SPE/$LiFePO_4$ cell delivers an inferior capacity. When transferring from 1 C to 0.1 C, both SPEs present a highly reversible discharge capacity without loss, suggesting there is no irreversible polarization during cycling. It is noteworthy that P-SPE have a more optimal capacity and rate performance due to the better interfacial compatibility and t_{Li^+}. The voltage distance (ΔV) between the charge and discharge curves represents the IR drops caused by the polarization. Fig. 4b illustrates the dependence of ΔV on cycling rates after fitting. It is obvious that the ΔV of Li/P-SPE/$LiFePO_4$ is smaller than that of the series one, indicating the less irreparable capacity and energy decay using the parallel electrolyte. The total resistance (R_b and polarization resistance) can be calculated to be 350 and 170 Ω for S-SPE and P-SPE *via* the slope of the relationship curves. Considering that the value of R_b is predominantly determined by the immanent properties of the electrolyte, the elevating of ΔV is largely originated from the concentration polarization as the current density increases. Due to the relatively high t_{Li^+}, the vicious impact on the capacity brought by the high discharge rates has been alleviated for P-SPE.

The cycling performance of the as-prepared $LiFePO_4$/Li batteries was then investigated at 0.2 C and 60 °C. As illustrated in Fig. 4c, the cells using S-SPE and P-SPE as electrolyte renders an initial discharge capacity of 135 mAh/g and 151 mAh/g, respectively. After 100 cycles, the retained capacity is 102 mAh/g with a declining rate of approximately 0.33 mAh/g per cycle for S-SPE. The capacity retention and columbic efficiency are 75 and 98%. By contrast, for Li/P-SPE/$LiFePO_4$, the declining rate is 0.29 mAh/g per cycle. It maintains a capacity of 128 mAh/g after 100 cycles with a capacity retention of 81%. In addition, the average columbic efficiency also proves to be above 99% apart from the initial cycle. From the comparison above, it is noticeable that the P-SPE achieves better reversibility and cyclability, though the ester groups in the two SPEs are both unstable against Li metal. This may result from the improved interfacial contact and ionic conductivity compared with S-SPE. Since interface impedance is an essential parameter for a high reversible battery, EIS was carried out before and after the cycling tests. Fig. S5 (Supporting information) depicts that R_i increases from 300 Ω to 1350 Ω for the S-SPE based cell. With respect to P-SPE, the initial R_i is smaller with a minor increase (from 164 Ω to 265 Ω), verifying the better cycling performance using P-SPE.

Moreover, the dendrite growth behavior of the batteries was also investigated by galvanostatic cycling of the symmetric Li/SPE/Li cells. As revealed in Fig. 4d, Li/S-SPE/Li exhibits an initial overpotential of 0.2 V and it gradually increases as further cycling. In stark contrast, the initial overpotential for Li/P-SPE/Li is 0.08 V, and there is no apparent magnifying even after 130 h. After polarization, the surface of lithium anode was scrutinized by SEM. As displayed in Figs. 4e and f, the morphology of the lithium electrode from the P-SPE based symmetric cell is flatter, suggesting that the planting and stripping process of lithium is uniform and highly reversible using P-SPE as the electrolyte. Here the interface compatibility is the fundamental factor that brings about the different polarization behavior. It is because P-P (PEGMA-IM) is more flexible that the contact between the anode and electrolyte becomes much compact and homogeneous. So the “hot spots” which are favorable for dendrite growth are less likely to be induced [38]. *Via* the discussion above and the comparison with other ether-linkage or PIL based electrolytes (listed in Table S2 in Supporting information), it can be concluded that the incorporation of ether linkage and imidazolium ionic liquid, especially the parallel structure, does make this SPE qualified for all-solid-state lithium metal batteries.

In summary, the multi-arm series/parallel structured PILs were fabricated *via* the ATRP of PEGMA-based monomer and the follow-up imidazolium grafting onto the four-arm initiator. P-P(PEGMA-IM) was corroborated to be more amorphous, and

the distribution of imidazolium groups and ether linkage onto different chains has a synergistic effect on the migration of lithium-ions. Superior to the series one, P-P(PEGMA-IM) presents an ionic conductivity of 0.489 mS/cm (60 °C) and a t_{Li^+} up to 0.46. The assembled Li/P-SPE/$LiFePO_4$ battery shows an initial discharge specific capacity of 151 mAh/g at 0.2 C, and the capacity retention rate reaches 81% after 100 cycles. By incorporating ILs into the multi-armed polymer backbone, our study reveals the significance of structural regulation on the modification of SPEs and broaden the approaches to design advanced SPEs for the next-generation energy storage devices.

Declaration of competing interest

The authors declare that they have no known competing financial interests or personal relationships that could have appeared to influence the work reported in this paper.

Acknowledgments

We are grateful to the National Natural Science Foundation of China (No. 51303083), the Natural Science Foundation of Jiangsu Province (No. BK20191293), and the Fundamental Research Funds for the Central Universities (No. 30920021123) for financial support.

Supplementary materials

Supplementary material associated with this article can be found, in the online version, at doi:10.1016/j.cclet.2021.08.031.

References

[1] D.H.S. Tan, A. Banerjee, Z. Chen, Y.S. Meng, Nat. Nanotech. 15 (2020) 170–180.
[2] C.Z. Zhao, B.C. Zhao, C. Yan, et al., Energy Storage Mater 24 (2020) 75–84.
[3] K. Qin, K. Holguin, M. Mohammadiroudbari, et al., Adv. Funct. Mater. 31 (2021) 2009694.
[4] Q. Wang, X. Liu, Z. Cui, et al., Electrochim. Acta 337 (2020) 135843.
[5] Z. Li, X.Y. Zhou, X. Guo, Energy Storage Mater. 29 (2020) 149–155.
[6] Q. Yu, K. Jiang, C. Yu, et al., Chin. Chem. Lett. 32 (2021) 2659–2678.
[7] D. Yu, X. Pan, J.E. Bostwick, et al., Adv. Energy Mater. 11 (2021) 2003559.
[8] J. Lai, Y. Xing, N. Chen, et al., Angew. Chem. Int. Ed. 59 (2020) 2974–2997.
[9] Q. Wang, L. Jiang, Y. Yu, J. Sun, Nano Energy 55 (2019) 93–114.
[10] Y. Xiao, Y. Wang, S.H. Bo, et al., Nat. Rev. Mater. 5 (2020) 105–126.
[11] X. Yuan, A.A. Razzaq, Y. Chen, et al., Chin. Chem. Lett. 32 (2021) 890–894.
[12] Q. Zhao, S. Stalin, C.Z. Zhao, L.A. Archer, et al., Nat. Rev. Mater. 5 (2020) 229–252.
[13] M. Kumar, S.S. Sekhon, Eur. Polym. J. 38 (2002) 1297–1304.
[14] H. Xu, P.H. Chien, J. Shi, et al., Proc. Natl. Acad. Sci. U. S. A. 116 (2019) 18815–18821.
[15] Z. Xiao, B. Zhou, J. Wang, et al., J. Membr. Sci. 576 (2019) 182–189.
[16] L. Porcarelli, C. Gerbaldi, F. Bella, J.R. Nair, et al., Sci. Rep. 6 (2016) 19892.
[17] L. Gao, J. Li, J. Ju, et al., Chem. Eng. J. 389 (2020) 124478.
[18] Z. Wan, D. Lei, W. Yang, et al., Adv. Funct. Mater. 29 (2019) 1805301.
[19] S. Xia, X. Wu, Z. Zhang, Y. Cui, W. Liu, Chem 5 (2019) 753–785.
[20] M.C. Long, T. Wang, P.H. Duan, et al., J. Energy Chem. 65 (2022) 9–18.
[21] W. Zha, W. Li, Y. Ruan, J. Wang, Z. Wen, Energy Storage Mater. 36 (2021) 171–178.
[22] Y. Lu, C.Z. Zhao, H. Yuan, et al., Adv. Funct. Mater. 31 (2021) 2009925.
[23] S.J. Tan, J. Yue, Y.F. Tian, et al., Energy Storage Mater. 39 (2021) 186–193.
[24] M. Forsyth, L. Porcarelli, X. Wang, N. Goujon, D. Mecerreyes, Acc. Chem. Res. 52 (2019) 686–694.
[25] Z. Shen, W. Zhang, G. Zhu, et al., Small Methods 4 (2020) 1900592.
[26] X. Zheng, T. Yang, J. Wei, C. Wang, M. Chen, J. Power Sources 496 (2021) 229843.
[27] Z. Xie, Z. Wu, X. An, et al., J. Membr. Sci. 596 (2020) 117739.
[28] X. Li, D. Wang, H. Wang, et al., ACS Appl. Mater. Interfaces 11 (2019) 22745–22753.
[29] Y. Zhu, J. Cao, H. Chen, Q. Yu, B. Li, J. Mater. Chem. A 7 (2019) 6832–6839.
[30] Z. Zeng, X. Chen, M. Sun, et al., Nano Lett. 21 (2021) 3611–3618.
[31] N. Zhou, Y. Wang, Y. Zhou, et al., Electrochim. Acta 301 (2019) 284–293.
[32] Y. Zhou, X. Xu, Z. Wang, et al., Phys. Chem. Chem. Phys. 22 (2020) 15734–15742.
[33] M. Herstedt, M. Smirnov, P. Johansson, et al., J. Raman Spectrosc. 36 (2005) 762–770.
[34] M. Li, L. Wang, B. Yang, T. Du, Y. Zhang, et al., Electrochim. Acta 123 (2014) 296–302.
[35] M.D. Tikekar, L.A. Archer, D.L. Koch, et al., Sci. Adv. 2 (2016) e1600320.
[36] J. Bao, G. Shi, C. Tao, et al., J. Power Sources 389 (2018) 84–92.
[37] A. Lasia, Electrochemical Impedance Spectroscopy and its Applications, Electrochemical Impedance Spectroscopy and its Applications,, Springer, Boston, 2002.
[38] Z. Yu, D.G. Mackanic, W. Michaels, et al., Joule 3 (2019) 2761–2776.